Available online at www.sciencedirect.com
ScienceDirect
European Journal of Mechanics B/Fluids 28 (2009) 88–102

Fluid–structure interaction of turbulent pulsatile flow within a flexible wall axisymmetric aortic aneurysm model

Khalil M. Khanafer [a,*], Joseph L. Bull [a], Ramon Berguer [a,b]

[a] *Vascular Mechanics Laboratory, Department of Biomedical Engineering, University of Michigan, Ann Arbor, MI 48109, USA*
[b] *Section of Vascular Surgery, University of Michigan, Ann Arbor, MI 48109, USA*

Received 3 August 2007; received in revised form 17 October 2007; accepted 17 December 2007

Available online 16 February 2008

Abstract

Pulsatile turbulent flow characteristics in an axisymmetric aortic aneurysm (AA) model were analyzed numerically using a simulated physiological waveform. The transport equations were solved using the finite element formulation based on the Galerkin method of weighted residuals. A fully-coupled fluid–structure interaction (FSI) analysis was utilized in this work. We investigated the effects of turbulent flow characteristics on the distribution of wall stress and flow patterns in AA models. Wall stress distributions were calculated by computational solid stress (CSS) model, which ignores the effect of the blood flow, and the FSI model that takes into account flow and solid mechanics. Our results showed that peak wall stress and peak deformation were found to occur shortly after peak systolic flow in the FSI model and at the peak luminal pressure condition in the CSS model. Further, CSS model underestimated wall stress calculations when compared to the FSI model. There were also significant differences in the structure of flow fields between the flexible and rigid wall aneurysm models. Contour plots of kinetic energy dissipation and the application of the Kolmogorov microscale suggest that the conditions that result in red blood cell damage and platelet activation most likely occur in the near-wall region of AA during turbulent flow.

Keywords: Aneurysm; Finite element; Flexible wall; Rigid wall; Turbulent

1. Introduction

Aortic aneurysms are the 14th leading cause of death in the US [1]. Most aortic aneurysms occur in the infrarenal abdominal aorta. From a flow mechanics standpoint, one can predict that changes in the geometry of an aortic aneurysm (AA) will results in changes in blood flow patterns within the aneurysm and in the hemodynamic stresses on its wall. Hemodynamic stresses associated with (or leading to) changes in the aortic wall that affect its mechanical integrity, result in aneurysm dilation and eventual rupture. Using computational techniques to calculate the hemodynamic stresses acting on aneurysm walls and to predict the likelihood of AA rupture is more accurate than the current practice of measuring the diameter changes in AA by ultrasound (US) or computed tomography (CT)

* Corresponding author.
E-mail address: khanafer@umich.edu (K.M. Khanafer).

0997-7546/$ – see front matter
doi:10.1016/j.euromechflu.2007.12.003

Nomenclature

AA	aortic aneurysm
d	non-dilated aortic diameter
D	maximum aneurysm diameter
$\ddot{d}_s$	acceleration of the solid region
E	Young's Modulus
$\mathbf{f}_f^B$	body force per unit mass
$\mathbf{f}_s^B$	externally applied body force vector at time
L	aneurysm length
L_{ent}	upstream length
L_{exit}	Downstream length
$\hat{n}$	normal direction
p	blood pressure
r	radial coordinate
Re_{max}	Maximum Reynolds number $(= du_{max}/\upsilon)$
t	time
$\boldsymbol{u}$	velocity vector
u_g	moving coordinate velocity
u_m	inlet mean velocity
z	longitudinal coordinate

Greek letters

ε	dissipation rate
ρ	fluid domain density
ρ_s	solid domain density
κ	Von Karman constant
μ	fluid dynamic viscosity
ω	turbulent frequency
$\sigma_1, \sigma_2, \sigma_3$	principal stresses
σ_f	fluid stress tensor
σ_s	solid Cauchy stress tensor
τ_f	fluid shear stress
τ_s	solid shear stress
υ	Poisson's ratio
υ	fluid kinematic viscosity ..... $(= \mu/\rho)$

Subscripts

f	fluid domain
∞	parameter evaluated at infinite shear rate
o	parameter evaluated at zero shear rate
s	solid domain

[2–7]. Numerical simulation allows for the study of conditions that are difficult or impossible to measure directly in humans or in animal models of AA.

Most studies of flow through aneurysms assume laminar flow [8–18], which typically occurs for Reynolds numbers less than 2000. However, turbulence was recorded in aortic aneurysm in humans by Bluth et al. [19]. In physical models of AA, it was found that the onset of turbulence is intermittent for Reynolds numbers between 2000 and 2600 [20,21]. These models had rigid walls and laminar inlet flow conditions [10,22,23]. There are few studies on the stability of flow and its transition to turbulence in AA. Yip and Yu [24,25] showed numerically that the onset of turbulence occurred at the distal neck of a large rigid wall AA model ($D/d = 4$) during the deceleration phase of the flow cycle. Ekaterinaris et al. [26] analyzed numerically steady laminar and turbulent flow in AA models. Their results showed that fluid shear stress is higher for turbulent flow than for laminar flow. Berguer et al. [27] developed a numerical model to analyze both laminar and turbulent pulsatile flows in aortic aneurysm models using physiological resting and exercise waveforms. They also compared hemodynamic stresses for non-Newtonian and Newtonian flows. The decreased stresses generated as a sequence of non-Newtonian effect were significant in realistic flow conditions. Recently, Khanafer et al. [28] numerically analyzed pulsatile turbulent flow, using simulated physiological rest and exercise waveforms, in axisymmetric-rigid AA models. Maximum turbulence-induced shear stress was found at the distal end of an AA model. In the large AA model (dilated to undilated diameter ratio = 3.33), at peak systolic flow velocity, fluid shear stress during exercise was 70.4% higher than at rest.

Turbulent flow is considered more damaging to the endothelial cells than laminar flow because kinetic forces are directed towards the vessel walls instead of being parallel to them, as occurs under laminar flow conditions. The unsteady turbulent shear stresses have been shown to damage the structural components of the endothelial cells lining the arterial wall, resulting in platelet aggregation and atherogenesis [29,30]. In addition to flow resistance, turbulence affects mass transport from the blood to the vessel, cell division and surface cell loss [31]. Turbulence also leads to countercurrents and pockets of sluggish flow which cause the buildup of thrombus in aneurysms. Therefore, turbulence, induced by sudden expansion of the flow stream as it enters the aneurysm, generates additional stresses on the aneurysm wall. These additional stresses may be responsible for further wall dilation, and eventually greater turbulence; possibly a self perpetuating mechanism for aneurysm growth. Given these significant consequences of turbulence shown in human AA, turbulence should be considered in the study of AA because it does exist in human aneurysms and by increasing mechanical wall stress, likely contributes to the growth and eventual rupture of an AA.

The FSI computational model we used coupled fluid and structural mechanics so that flow-induced stresses and pressure-induced deformations in the aneurysm wall are computed simultaneously. The few studies of AA with FSI that have been reported have all assumed laminar flow. Scotti et al. [14], utilizing the FSI model and laminar flow conditions, studied the effects of asymmetry and wall thickness on the flow patterns and the wall dynamics of aneurysms. They concluded that asymmetric aneurysms are exposed to higher mechanical stresses than symmetric aneurysms. Di Martino et al. [8] simulated numerically the presence of thrombus in the lumen and the mechanical interaction between laminar blood flow and wall dynamics in a 3D aneurysm. Recently, Wolters et al. [17] described a patient-specific computational model of fluid–structure interaction in abdominal aortic aneurysm under laminar flow assumption.

But previous studies have established that flow is not laminar within AA throughout the cardiac cycle: flow is turbulent for a fraction of the cycle and laminar for the remainder of it [10,22,32]. This study investigated the effects of wall flexibility and transient turbulent flow on the resulting flow patterns and wall mechanics, using a FSI model. We also compared wall stress and deformation values between the FSI and the CSS models (the latter ignores the inertial and viscous effects of blood flow through the aneurysm).

2. Mathematical formulation for FSI and CSS models

Turbulent, Newtonian blood flow with a density of 1050 kg/m^3 and a viscosity of 0.00345 N s/m^2 was studied in an idealized axisymmetric aneurysm as depicted in Fig. 1. The following nomenclature was used: length of the aneurysm $= L$, aneurysm maximum diameter $= D$, and un-dilated aortic diameter $= d$ ($d = 2.5$ cm). The dilation of the aneurysm was $D/d = 2.5$ and the dimensionless length was set at $L/d = 4$. The original virtual aneurysm model was approximated by using the following function as follows:

$$f(z) = \frac{D-d}{4}\left[1 + \sin\left(\frac{2\pi z}{L} - \frac{\pi}{2}\right)\right] + \frac{d}{2} \tag{1}$$

Due to the limitations of CT scan imaging, the average wall thickness of the aneurysm is set to 1.5 mm based on measurements by Raghavan et al. [33], Vorp et al. [34] and Thubrikar et al. [35].

FSI analysis. An arbitrary Lagrangian–Eulerian formulation was employed to describe the fluid motion in the FSI model. The governing equations for the fluid domain are the continuity and Navier–Stokes equations described as:

$$\begin{aligned} &\nabla \cdot \mathbf{u} = 0 \\ &\rho_{\mathrm{f}} \frac{\partial \mathbf{u}}{\partial t} + \rho_{\mathrm{f}}(\mathbf{u} - \mathbf{u}_{\mathrm{g}}) \cdot \nabla \mathbf{u} = \nabla \cdot \boldsymbol{\sigma}_{\mathrm{f}} + \rho_{\mathrm{f}} \mathbf{f}_{\mathrm{f}}^{\mathrm{B}} \end{aligned} \tag{2}$$

where $\mathbf{u}$ is the fluid velocity vector, ρ_{f} is the fluid density, $\mathbf{u}_{\mathrm{g}}$ is the moving coordinate velocity, $\mathbf{f}_{\mathrm{f}}^{\mathrm{B}}$ is the body force per unit volume, $(\mathbf{u} - \mathbf{u}_{\mathrm{g}})$ is the relative velocity of the fluid with respect to the moving coordinate velocity, and $\boldsymbol{\sigma}_{\mathrm{f}}$ is the fluid stress tensor. The governing equation for the solid domain of the FSI model can be described by the following elastodynamics equation:

$$\rho_{\mathrm{s}} \ddot{\mathbf{d}}_{\mathrm{s}} = \nabla \cdot \boldsymbol{\sigma}_{\mathrm{s}} + \mathbf{f}_{\mathrm{s}}^{\mathrm{B}} \tag{3}$$

where ρ_{s} is the AA wall density, $\boldsymbol{\sigma}_{\mathrm{s}}$ is the solid Cauchy stress tensor, $\mathbf{f}_{\mathrm{s}}^{\mathrm{B}}$ is the externally applied body force vector at time t and $\ddot{\mathbf{d}}_{\mathrm{s}}$ represents the local acceleration of the solid region ($\ddot{\mathbf{d}}_{\mathrm{s}} = \dot{\mathbf{u}}_{\mathrm{g}}$). The AAA wall is assumed to be a non-linear, isotropic, hyperelastic material with a density of 2200 kg/m^3, a Young's Modulus $E = 2.7$ MPa and a Poisson's ratio $\upsilon = 0.45$. For hyperelastic materials, the strain-energy function based on Mooney–Rivlin material model is given as

$$W = \alpha(I_{\mathrm{B}} - 3) + \beta(I_{\mathrm{B}} - 3)^2 \tag{4}$$

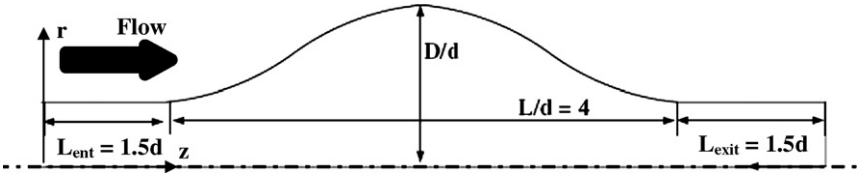

Fig. 1. Axisymmetric idealized abdominal aortic aneurysm model.

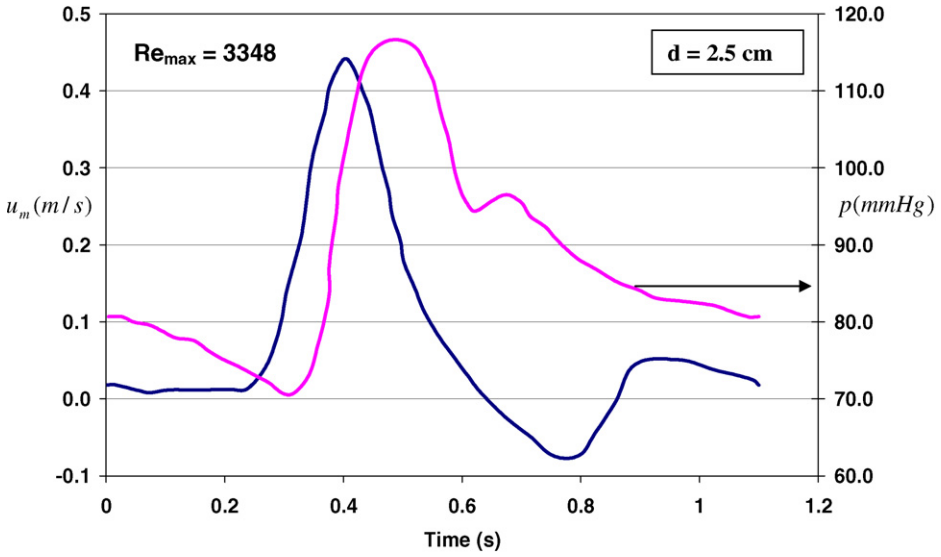

Fig. 2. Pulsatile inlet mean velocity waveform and outlet pressure waveforms based on in-vivo recording. Inlet peak systolic flow occurs at $t = 0.4$ s and exit peak systolic pressure at $t = 0.5$ s [37].

where W is the strain-energy density, B is the left Cauchy–Green tensor, and I_B is the first invariant of B; α and β are the model parameters indicative of the mechanical properties of aneurysm wall. The material parameters $\alpha = 17.4$ N/cm^2 and $\beta = 188.1$ N/cm^2 are based on the means of the best-fit material parameters of the data examined by Raghavan and Vorp [36]. The bulk modulus (κ_{MR}) for the mooney-Rivlin model is determined as:

$$\kappa_{MR} = \frac{E}{3(1-2\upsilon)} \tag{5}$$

Boundary Conditions. We specified the following boundary conditions for the fluid domain: symmetry about the centerline, time dependent fully developed turbulent velocity at the inlet and a time dependent normal traction at the exit of the fluid domain. These boundary conditions were depicted in the following mathematical form:

$$\left.\begin{aligned} &\frac{\partial u_z}{\partial r} = u_r = 0 && \text{at } r = 0 \\ &u_z(r,t) = 1.22u_m(t)\left[1-\left(\frac{2r}{d}\right)\right]^{1/7}, \quad u_r = 0 && \text{at } z = 0 \\ &\sigma_{nn} = \hat{n}\cdot p(t) I \cdot \hat{n} && \text{at } z = L_e \end{aligned}\right\} \tag{6}$$

where σ_{nn} is the normal traction, $\hat{n}$ is the normal vector, and I is the identity matrix. In contrast to steady flow studies, *in vitro* and computational studies of pulsatile blood flow require the specification of the inlet mean velocity $u_m(t)$ and pressure $p(t)$ waveforms at the inlet and exit of the fluid domain shown in Fig. 2. The velocity waveform and the exit pressure waveforms were reported by Mills et al. [37] corresponding to $Re_{max} = 3348$. The maximum Reynolds number was defined as

$$Re_{max} = \frac{\rho u_{max} d}{\mu} \tag{7}$$

where u_{max} is the maximum inlet mean velocity (Fig. 2) and μ is the viscosity. The boundary conditions on both ends of the solid domain impose zero translation in the axial direction. The outer-wall surface of the solid domain was subject to a zero normal traction assuming that the surrounding tissues do not exert any external forces, pressures, or tethering on the arterial wall [5]. The boundary conditions at the interface between the fluid domain and the solid domain are summarized as follows:

$$\left.\begin{aligned} &\text{Displacement:} && \mathbf{d}_f = \mathbf{d}_s \\ &\text{Traction:} && \boldsymbol{\sigma}_f = \boldsymbol{\sigma}_s \\ &\text{No-slip:} && \mathbf{u} = \mathbf{u}_g \end{aligned}\right\} \tag{8}$$

where $\mathbf{d}$, $\boldsymbol{\sigma}$, $\mathbf{n}$ are the displacement vector, stress tensor, and normal vector, respectively. The subscripts s and f indicate fluid and solid properties, respectively.

CSS analysis. For the CSS analysis, the effect of blood flow is ignored and a spatially uniform luminal pressure waveform from Fig. 2 is applied onto the inner wall of the aneurysm. The solid wall of the aneurysm is only utilized with prescribed zero translation at the proximal and distal ends, and with a pressure boundary condition given by

$$\sigma_{nn} = \hat{n} \cdot p(t) I \cdot \hat{n} \tag{9}$$

3. Turbulence modeling

Wilcox's κ–ω model [38] was used in this study because it accurately models pulsatile flow that encompasses laminar, transitional, and turbulent regimes [39,40]. This model has been found to perform better than other turbulence models when compared against experimental data [41]. The Wilcox κ–ω model was primarily intended for simulating globally low-*Re* internal flows. There is evidence in the literature to suggest that the Wilcox κ–ω model performs better than the standard κ–ε model for flows involving deceleration and/or separation resulting from adverse pressure gradients. Lee et al. [42] verified that in the laminar flow region, the numerical predictions by κ–ω turbulence model matched those by the laminar flow modeling with good accuracy. Varghese and Frankel [40] showed that the κ–ω model was in much better agreement with previous experimental measurements than the RNG κ–ε and the standard κ–ε models. The prediction of transition and turbulence in low-*Re* number flows is important when simulating the flow in aneurysms. The model transport equations for turbulent kinetic energy (κ) and turbulence frequency (ω) in the Wilcox model are as follows,

$$\rho\frac{\partial \kappa}{\partial t} + \rho u_j \frac{\partial k}{\partial x_j} + \frac{\partial}{\partial x_j}\left[\left(\mu + \frac{\mu_t}{\sigma_k}\right)\frac{\partial k}{\partial x_j}\right] - \rho\overline{u_i' u_j'}\frac{\partial u_j}{\partial x_i} - \rho\beta^* \omega\kappa \tag{10}$$

and

$$\rho\frac{\partial \omega}{\partial t} + \rho u_j \frac{\partial \omega}{\partial x_j} + \frac{\partial}{\partial x_j}\left[\left(\mu + \frac{\mu_t}{\sigma_\omega}\right)\frac{\partial \omega}{\partial x_j}\right] - \alpha\frac{\omega}{\kappa}\left(\rho\overline{u_i' u_j'}\frac{\partial u_j}{\partial x_i}\right) - \rho\beta\omega^2 \tag{11}$$

where $\sigma_\kappa = \sigma_\omega = 2$, $\beta^* = 0.072$, $\beta = 0.072$, and $\alpha = 1.0$. Using the κ–ω model, the eddy viscosity is modeled as:

$$\mu_t = \rho\frac{\kappa}{\omega}$$

The κ–ω model also has a transitional variant, which is of special interest to us since the AA blood flow is not fully turbulent in the entire domain or throughout the entire pulse cycle. The transitional κ–ω model is similar to the standard model, but with some modifications. The most important modification is the low-*Re* correction factor applied to the eddy viscosity

$$\mu_t = \alpha^* \frac{\rho\kappa}{\omega} \tag{12}$$

The coefficient α^* damps the turbulent viscosity causing a low-Reynolds-number correction. It is given by

$$\alpha^* = \alpha_\infty^*\left(\frac{\alpha_0^* + Re_t/R_\kappa}{1 + Re_t/R_\kappa}\right) \tag{13}$$

Where $Re_t = \rho\kappa/\mu\omega$, $R_\kappa = 6$, $\alpha_0^* = \beta_i/3$, $\beta_i = 0.072$. Note that, in the high-Reynolds-number form of the κ–ω model, $\alpha^* = \alpha_\infty^* = 1$ (Wilcox [38]). The transport equations for κ and ω remain as in Eqs. (10) and (11), with the exception of the addition of the low-*Re* correction in the eddy viscosity and the modification of some coefficients to make them functions of the local flow structure. In the κ equation, the coefficient on the dissipation term becomes:

$$\beta^* = \beta_\infty^*\left(\frac{4/15 + (Re_t/R_\beta)^4}{1 + (Re_t/R_\beta)^4}\right) \tag{14}$$

where $R_\beta = 8$ and $\beta_\infty^* = 0.09$. In the ω equation, the production coefficient takes the form:

$$\alpha = \frac{\alpha_\infty}{\alpha^*}\left(\frac{\alpha_0 + Re_t/R_\omega}{1 + Re_t/R_\omega}\right) \tag{15}$$

where $R_\omega = 2.95$, $\alpha_\infty = 0.52$ and $\alpha_0 = 1/9$.

4. Numerical scheme

A finite element formulation based on the Galerkin method was employed to solve the governing equations of fluid–structure interaction model in abdominal aortic aneurysm using ADINA software (v8.3.1, ADINA R&D, Inc., Watertown, MA) subject to the boundary conditions described above. The finite element method was used to discretize the continuity and momentum equations. These equations are weighted with the virtual quantities of pressure and velocities. The Newton–Raphson method was used to solve the discretized equations for the fluid and solid regions. A time step size of 5×10^{-3} second was used until periodic convergence solution is achieved after 3 cycles. When the relative change in variables between consecutive iterations was less than 10^{-4}, convergence was assumed to have been achieved. The simulations were performed on a PC using 1.73 GHz processor and 1 GB of RAM.

Many numerical experiments of various mesh sizes were performed to achieve grid-independent results and to determine the best compromise between accuracy and minimizing computer execution time. As such, a variable grid-size system was employed in the present work to capture the rapid changes in the dependent variables especially near the wall where the major gradients occur inside the boundary layer. To test and assess grid independence of the solution scheme, numerical experiments were performed using different mesh sizes (1350 4-node elements, 3500 4-node elements, and 7200 4-node elements). Based on the results, a mesh size of 3500 4-node elements (non-uniform spacing) was adopted for all the cases completed in the present study. Further increase of the mesh size did not significantly change the final results (Fig. 3).

5. Model validation

We validated our numerical results against the analytical results of Harris [43] of the absolute mid-span displacement of a pipe due to internal fluid flow and gravity, and both results were found to be in excellent agreement as shown in Fig. 4. As an additional check on the accuracy of our work, the present code was validated against experimental and numerical results found in the literature [44,45] for Newtonian axial velocity profile in a pipe normalized by centerline velocity at $Re = 4000$, as depicted in Fig. 5. Fig. 5 illustrates an excellent agreement between our results and experimental results of Shemer et al. [45]. Furthermore, velocity profile across the center of an aneurysm was compared between our results and the numerical and experimental results of Budwig et al. [21] as depicted in Fig. 6 and the correlation is excellent.

6. Results and discussion

6.1. Comparison of wall stresses between FSI and CSS models

Table 1 and Fig. 7 show the relevance of the FSI model compared with the CSS model (ignores blood flow) in calculating peak wall stress and peak displacement in a flexible wall aneurysm model. The values we computed for the stresses are comparable to those published in the literature [3]. Table 1 shows a comparison of peak wall stress between FSI and CSS models. The CSS model ignores the effect of blood flow and applies the temporal variation of intraluminal pressure acting on the inner wall of the aneurysm to calculate AA wall stresses. The CSS model predicts lower value of peak wall stress than the FSI model by 8% at $t = 0.45$ s (Table 1). This is due to the effect of the inertial forces generated by the flow on the walls of the aneurysm. Table 1 shows an interesting result associated with the occurrence of peak wall stress and peak displacement. Peak wall stress and peak displacement take place during $0.4\text{ s} < t < 0.5$ s in the FSI model and at $t = 0.5$ s in the CSS model. This is associated with the phase delay (0.1 s)

Table 1
Comparison of peak wall stress (N/cm^2) at different times of the cycle between FSI and Transient Solid Mechanics Model

Model	Time = 0	Time = 0.45* s	Time = 0.5 s (Peak Luminal Pressure)
Fluid–Structure Interaction (FSI)	25.7	40.5	37.6
Computational Solid Stress (CSS)	25.5	37.5	39.6

* This time corresponds to the occurrence of peak wall stress in FSI analysis.

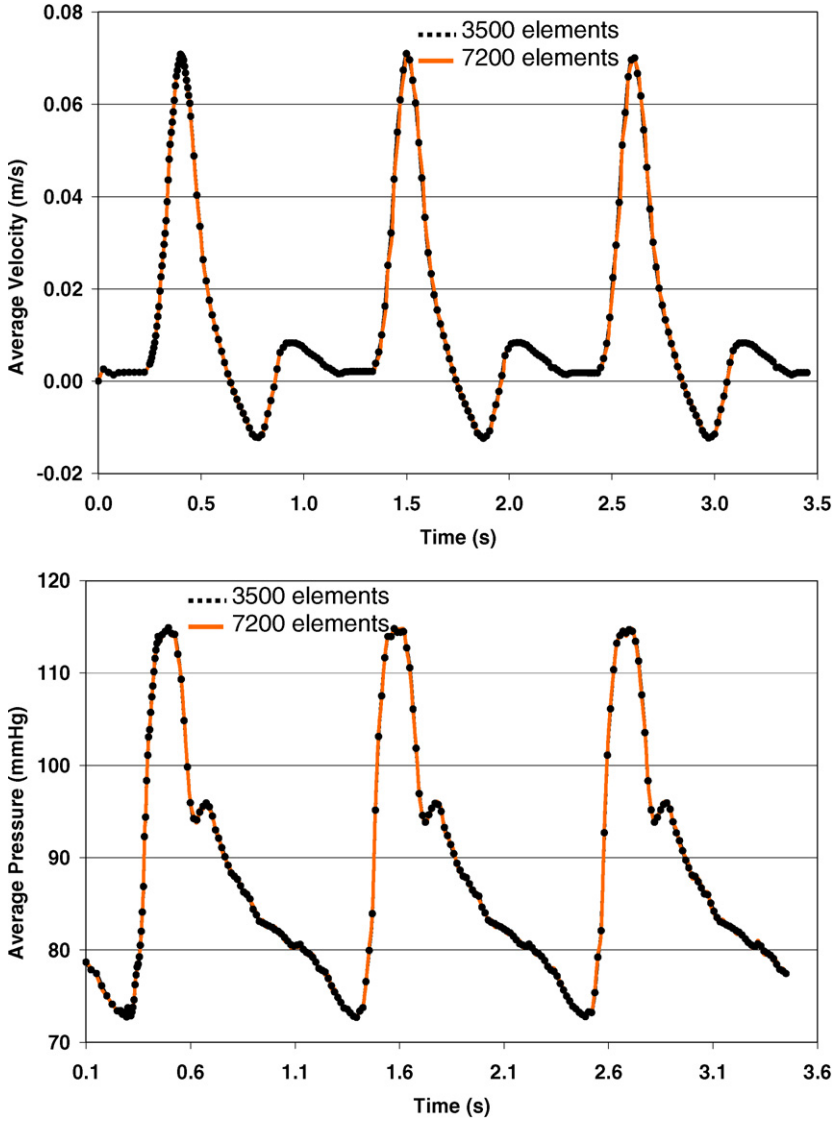

Fig. 3. Effect of the mesh size on the temporal variation of the average velocity and average pressure calculated along a plane passing through the middle of the aneurysm.

between the peak inlet velocity ($t = 0.4$ s) and peak exit pressure ($t = 0.5$ s). Thus, maximum deformation occurs ($t = 0.46$ s) after peak systole flow condition ($t = 0.4$ s) as demonstrated in Fig. 7 which represents a comparison of the temporal variation of the peak displacement between the FSI and CSS models. This is due to the fact that the effect of the velocity and traction boundary conditions is not instantly transmitted to the walls of aneurysm in FSI model. Fig. 7 shows high oscillations in the deformation in the CSS model. These oscillations are not seen in the FSI model due to the viscous damping effect of flow.

6.2. *Comparison of flow patterns and global power between flexible and rigid-wall models*

Fig. 8 illustrates a comparison of the streamline contours in the flexible wall model and rigid wall aneurysm model for various scenarios of the flow conditions. Fig. 8 shows that the flow structure in the flexible wall model is different from the results of a rigid wall aneurysm model. As the flow starts to decelerate soon after the peak flow at peak luminal pressure, a large vortex develops at the proximal end of the AA in the rigid wall model while the flexible wall

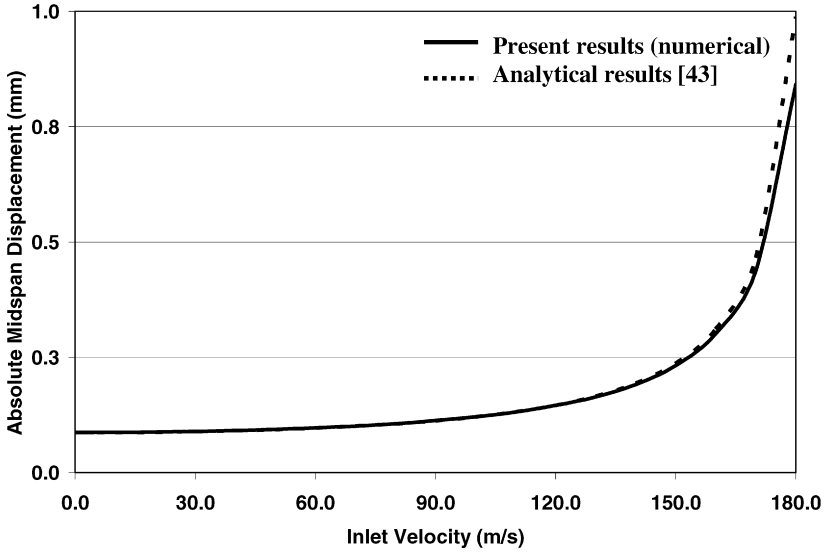

Fig. 4. Comparison of the absolute mid-span displacement of a pipe due to internal fluid flow and gravity as determined by our present work and the analytical results of Harris [43].

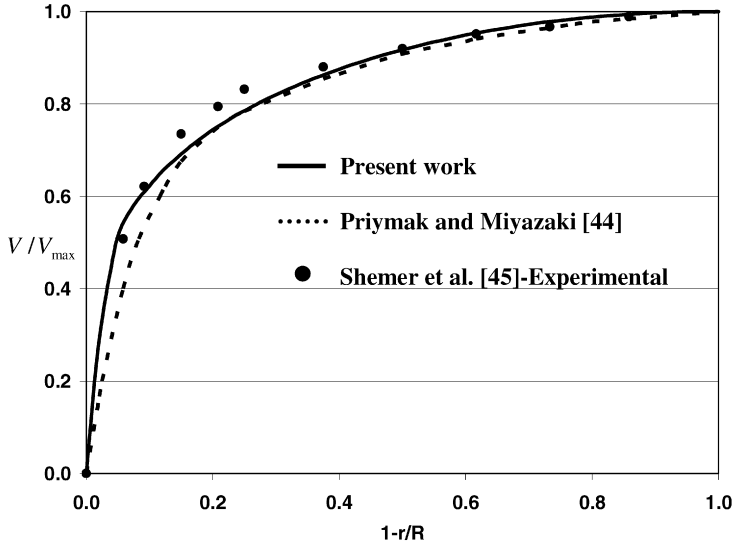

Fig. 5. Comparison of Newtonian turbulent normalized axial velocity between present result and other results in the literature ($Re = 4000$).

model exhibits a small vortex at the proximal end of the aneurysm due to the elastic energy stored in the expanding compliant wall. In both models, as the flow continues to decelerate the vortices increase in size and move downstream during the retrograde flow period of the cycle

Fig. 9 illustrates a comparison of the temporal variation of the global power involved during a cardiac cycle between flexible wall model and rigid wall model. The global power calculations are based on the inlet and outlet pressure waveforms and the corresponding flow rate waveforms (Power $= Q_{\text{out}} P_{\text{out}} - Q_{\text{in}} P_{\text{in}}$) [46]. Fig. 9 shows an interesting result associated with global power at peak flow condition for both models. The flexible wall model exhibits higher power than rigid wall model at peak flow condition to expand the aneurysm walls. This is associated with the fact that there is only fluid viscous dissipation in the case of rigid model, while there is also viscoelastic dissipation which is more significant in the case of flexible model. Therefore, kinetic energy is absorbed by the walls during the acceleration phase in the form of potential energy to expand the walls while during the deceleration phase the stored energy is restored and the walls contract.

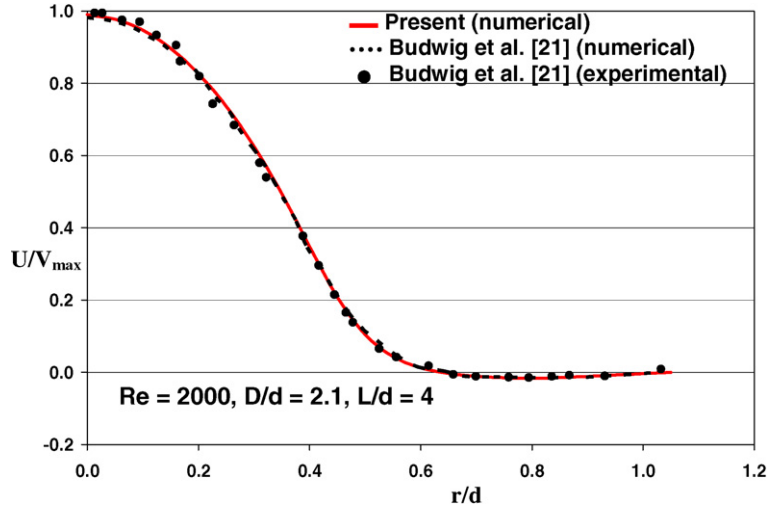

Fig. 6. Comparison of steady velocity profiles across the center of the aneurysm between the present results and that of Budwig et al. [21].

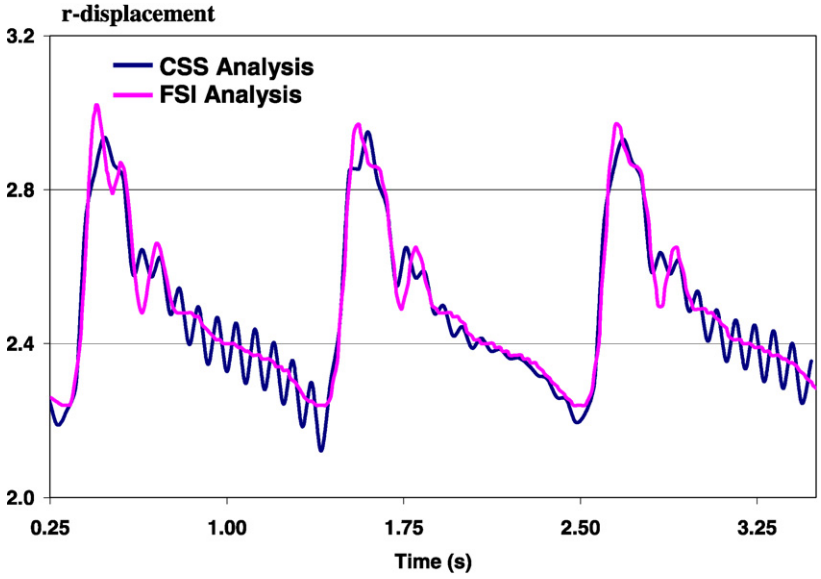

Fig. 7. Comparison of the maximum r-displacement between FSI analysis and transient CSS analysis.

The time evolution of the average exit velocity and inlet pressure for rigid and flexible wall models is shown in Fig. 10. The flexible wall model exhibits lower exit average velocity and higher inlet pressure than the rigid wall model at peak flow condition. This is due to the combined effect of the expanding walls of the aneurysm and the phase delay between the peak inlet velocity and peak exit pressure. In addition, Fig. 10(a) shows that the exit peak velocity in the flexible wall model occurs ($t = 0.47$) later than in the rigid wall aneurysm model ($t = 0.4$ s). However, the exit peak velocity in the rigid wall aneurysm model occurs at the same time as the inlet peak velocity.

6.3. Wall stress distribution in the flexible wall model under turbulent flow

The effect of the flow dynamics on the AA wall stress distribution (Fig. 11) is measured in terms of Von Mises stress which refers to the maximum distortion energy criterion. Von Mises stress is defined as a function of the principal

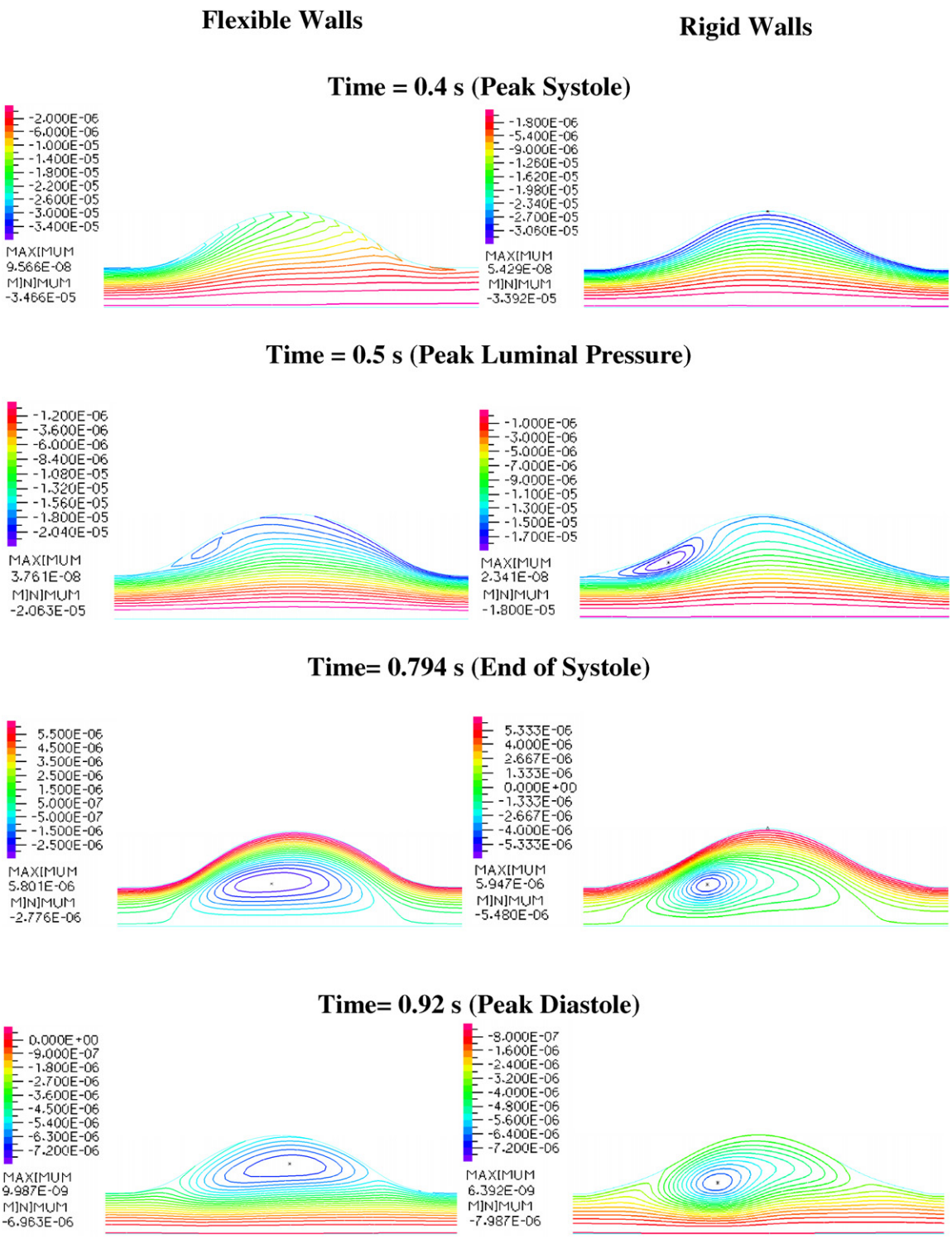

Fig. 8. Comparison of streamlines within aneurysms of flexible and rigid walls under transient turbulent flow condition. Flow direction from left-to-right.

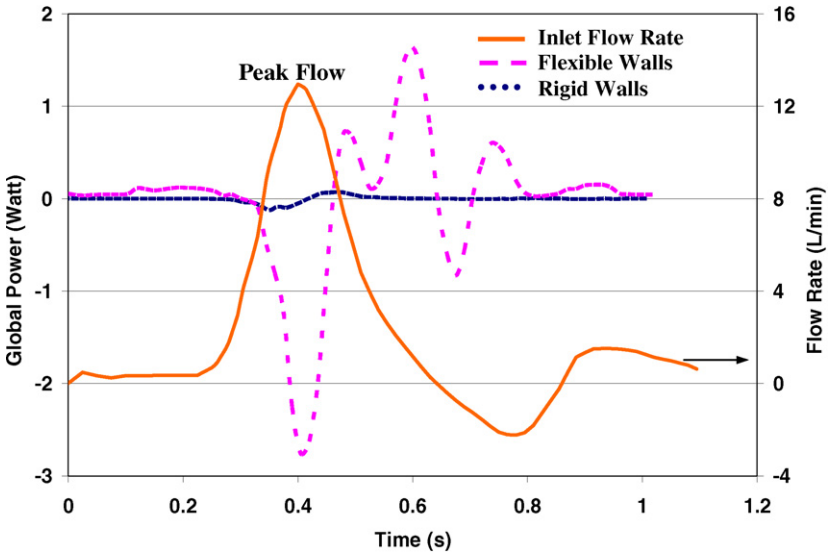

Fig. 9. Comparison of the temporal variation of the global power between rigid model and compliant model.

stresses σ_1, σ_2, and σ_3, as follows:

$$\sigma_{VM} = \sqrt{\frac{(\sigma_1 - \sigma_2)^2 + (\sigma_1 - \sigma_3)^2 + (\sigma_2 - \sigma_3)^2}{2}} \tag{16}$$

As mentioned earlier, peak wall stress does not occur at peak systolic flow condition or at peak luminal pressure, but rather during the time interval 0.4 s $< t <$ 0.5 s. This is because there is a phase delay between peak systolic flow condition and peak luminal pressure condition.

6.4. Comparison of the turbulence kinetic energy and viscous dissipation rate between flexible and rigid wall aneurysms

Comparison of the turbulence kinetic energy and turbulent frequency between flexible and rigid wall aneurysms at peak pressure is shown in Fig. 12. Fig. 12 illustrates that the turbulence kinetic energy and turbulence frequency fields are confined to narrow regions at the proximal and distal regions of the aneurysm. The rigid wall aneurysm exhibits larger turbulence kinetic energy and turbulence frequency than the flexible wall model. Cyclic turbulent stresses in flowing blood are known to alter the structure of the arterial wall and may also cause damage to red blood and endothelial cells and local activation of platelets. The smallest turbulent eddies (Kolmogorov microscale), which are a function of the kinematic viscosity of blood and turbulent dissipation rate, can mechanically damage the blood cells and the components of the arterial wall. Liu and Lu [47] pointed out that eddies with a Kolmogorov microscale up to 10 times the size of red blood cell (that have an average diameter of 8 μm) can be regarded as biomechanically damaging to the blood cells and endothelial cells. The Kolmogorov microscale is defined as

$$\eta = \left(\frac{\nu^3}{\varepsilon}\right)^{1/4} \tag{17}$$

where ν is the kinematic viscosity of blood and ε is the dissipation rate. From Fig. 12, in the FSI model, the Kolmogorov microscale length is estimated to be about 87.15 μm at the distal end of the aneurysm and 108.4 μm at the proximal end. The smallest scale (87.15 μm) is within the limit of 10 times the mean diameter of red blood cell. Since the smallest turbulent eddies were located inside a narrow region along the AA wall, red blood cell damaging and platelet activating are likely to occur inside that region. In the rigid wall model, (Fig. 12) the dissipation rate was confined to a narrow region around the distal end and proximal end of the aneurysm. The Kolmogorov length scales are estimated around 51.7–77.2 μm in that particular zone. This range is well within the limit of 10 times the average diameter of a red blood cell which causes significant damage to the endothelial cells. The rigid wall aneurysm model overestimates the Kolmogorov scale compared to the flexible wall model.

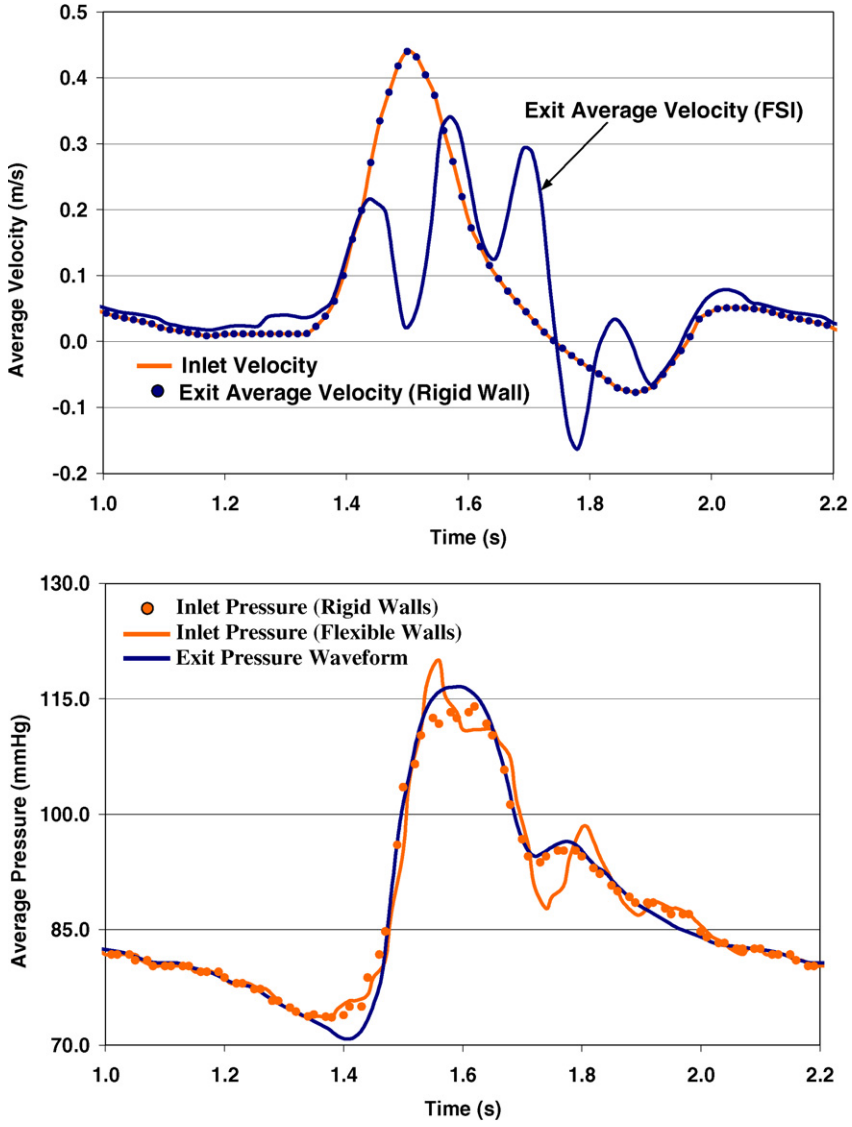

Fig. 10. (a) Temporal variation of the average velocity and (b) temporal variation of the average pressure at the inlet and exit of the aneurysm.

6.5. Limitation

The present study has some limitations since our model did not include the iliac bifurcation and the possibility of thrombus within the AA. The iliac bifurcation usually causes pressure wave reflection resulting in transient increase in pressure within the AA. Intraluminal thrombus frequently found in AA may contribute to wall stress reduction. The assumption of uniform wall thickness is another limitation of this work. Clinical observations suggest that variable thickness of the arterial wall around the aneurysm which may affect the value of the maximum wall stress and its location. These effects will be considered in future work.

7. Conclusion

We investigated an FSI model of AA under pulsatile turbulent flow conditions. The CSS analysis (i.e. ignores blood flow) of AA wall mechanics can be used to approximate wall stresses. However, the flexible wall analysis provides a more accurate computation of flow and pressure fields within the aneurysm simultaneously with the mechanics of

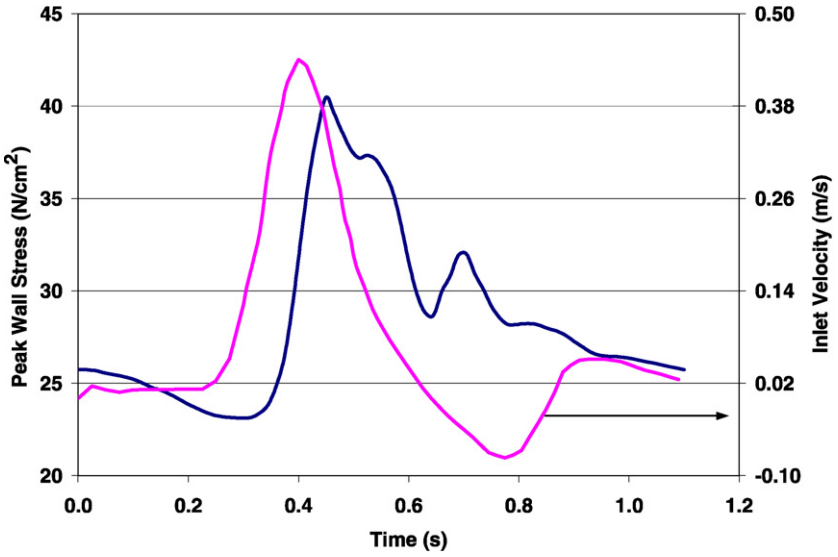

Fig. 11. Temporal variation of peak wall stress in FSI model under turbulent flow condition.

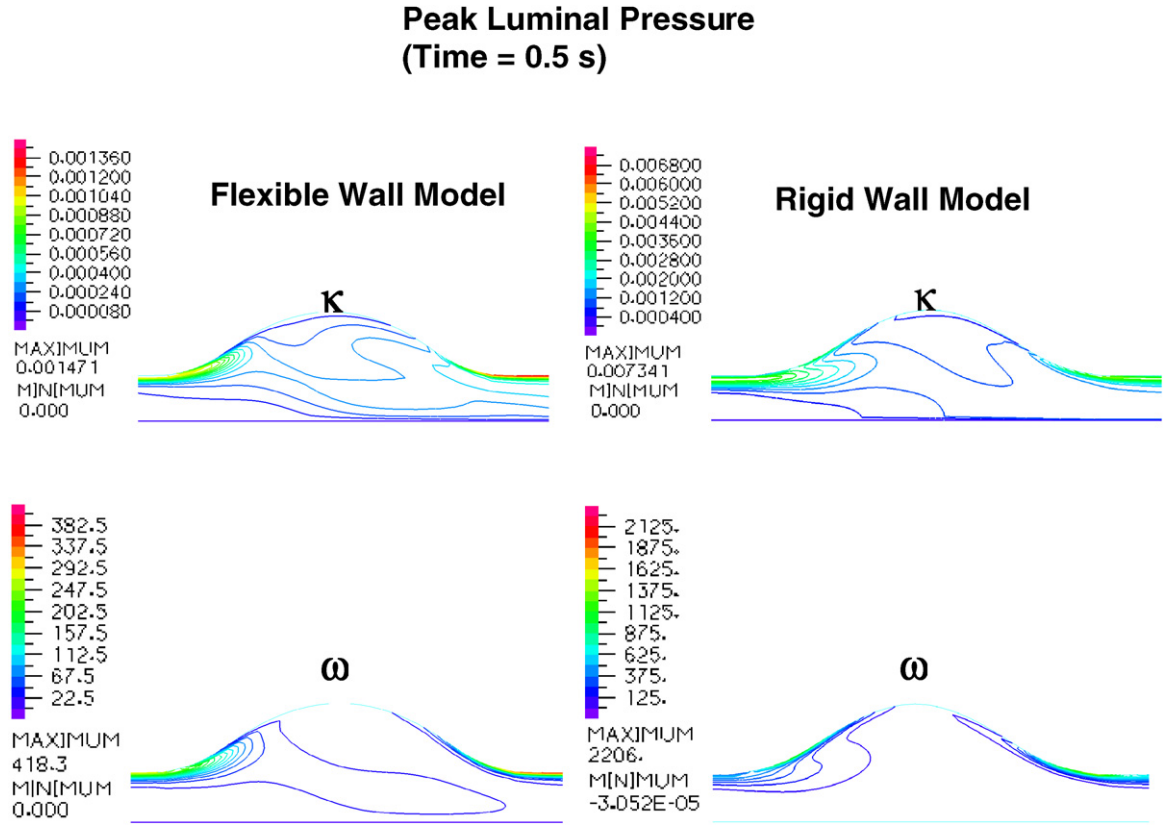

Fig. 12. Comparison of the turbulence kinetic energy and turbulence frequency between flexible walls and rigid walls aneurysm.

its wall. Our work also shows that the flow structure in the numerical model depends on whether the aneurysm wall model is rigid or flexible. We have also shown that peak wall stress and peak deformation occur shortly after systolic peak flow velocity in the flexible wall model while in the CSS model they take place at peak pressure. Due to the

collision of the vortices with the wall that cause it to vibrate, local pressure increases which contributes to wall shear stress increase and weakening of the AA wall. The present work represents the first computational study to analyze turbulent pulsatile flow within compliant walls of an aneurysm and to determine realistic aneurysm wall stress values.

Acknowledgement

This work was supported by the Frankel Vascular Research Fund.

References

[1] R.F. Gillum, Epidemiology of aortic aneurysm in the United States, J. Clinical Epidemiology 48 (1995) 1289–1298.
[2] E.S. Di Martino, D.A. Vorp, Effect of variation in intraluminal thrombus constitutive properties on abdominal aortic aneurysm wall stress, Ann. Biomed. Eng. 31 (2003) 804–809.
[3] M.F. Fillinger, S.P. Marra, M.L. Raghavan, F.E. Kennedy, Prediction of rupture risk in abdominal aortic aneurysm during observation: Wall stress versus diameter, J. Vasc. Surg. 37 (2003) 724–732.
[4] M.F. Fillinger, M.L. Raghavan, S.P. Marra, J.L. Cronenwett, F.E. Kennedy, In vivo analysis of mechanical wall stress and abdominal aortic aneurysm rupture risk, J. Vasc. Surg. 36 (2002) 589–597.
[5] W.R. Mower, W.J. Quinonse, S.S. Gambhir, Effect of intraluminal thrombus on abdominal aortic aneurysm wall stress, J. Vasc. Surg. 26 (1997) 602–608.
[6] M.L. Raghavan, D.A. Vorp, M.P. Federle, M.S. Makaroun, M.W. Webster, Wall stress distribution on three-dimensionally reconstructed models of human abdominal aortic aneurysm, J. Vasc. Surg. 31 (2000) 760–769.
[7] A.K. Venkatasubramaniam, M.J. Fegan, T. Mehta, K.J. Mylankal, B. Ray, G. Kuhan, I.C. Chetter, P.T. McCollum, A comparative study of aortic wall stress using finite element analysis for ruptured and non-ruptured abdominal aortic aneurysms, Eur. J. Vasc. Endovasc. Surg. 28 (2004) 168–176.
[8] E. Di Martino, G. Guadagni, A. Fumero, G. Ballerini, R. Spirito, P. Biglioli, et al., Fluid–structure interaction within realistic three-dimensional models of the aneurysmatic aorta as a guidance to assess the risk of rupture of the aneurysm, Med. Eng. Phys. 23 (2001) 647–655.
[9] D.F. Elger, J.B. Slippy, R.S. Budwig, T.A. Kraishi, K.H. Johansen, A numerical study of the hemodynamics in a model AAA, Proc. ASME FED symposium on Bio-Medical Fluids Engineering 212 (1995) 5–22.
[10] C.J. Egelhoff, R.S. Budwig, D.F. Elger, T.A. Khraishi, K.H. Johansen, Model studies of the flow in abdominal aortic aneurysms during resting and exercise conditions, J. Biomech. 32 (1999) 1319–1329.
[11] E.A. Finol, C.H. Amon, Blood flow in abdominal aortic aneurysms: Pulsatile flow hemodynamics, ASME, J. Biomech. Engr. 123 (2001) 474–484.
[12] E.A. Finol, C.H. Amon, Flow-induced wall shear stress in abdominal aortic aneurysms: Part I – Steady flow hemodynamics, Computer Methods Biomech. Biomed. Eng. 5 (2002) 309–318.
[13] E.A. Finol, K. Keyhani, C.H. Amon, The effect of symmetry in abdominal aortic aneurysms under physiologically realistic pulsatile flow conditions, ASME J. of Biomech. Eng. 125 (2003) 207–217.
[14] C.M. Scotti, A.D. Shkolnik, S.C. Muluk, E.A. Finol, Fluid–structure interaction in abdominal aortic aneurysms: Effects of asymmetry and wall thickness, BioMedical Engineering OnLine 4 (2005) 1–22.
[15] T.W. Taylor, T. Yamaguchi, Three-dimensional simulation of blood flow in an abdominal aortic aneurysm-steady and unsteady flow cases, ASME J. Biomech. Engr. 116 (1993) 89–98.
[16] N. Viswanath, C.M. Rodliewicz, S. Zajac, On the abdominal aortic aneurysms: pulsatile state considerations, Med. Eng. Phys. 19 (1997) 343–351.
[17] B.J. Wolters, M.C. Rutten, G.H. Schurink, J. Kose, J. de Hart, F.N. van de Vosse, A patient-specific computational model of fluid–structure interaction in abdominal aortic aneurysms, Med. Eng. Phys. 27 (2005) 871–883.
[18] K. Khanafer, P. Gadhoke, R. Berguer, J.L. Bull, Modeling pulsatile flow in aortic aneurysms: Effect of non-Newtonian blood, Biorheology 43 (2006) 661–679.
[19] E.L. Bluth, S.M. Murphey, L.H. Hollier, M.A. Sullivan, Color flow Doppler in the evaluation of aortic aneurysms, Int. Angiol. 9 (1990) 8–10.
[20] D. Bluestein, L. Niu, R.T. Schoephoerster, M.K. Dewanjee, Steady flow in an aneurysm model: Correlation between fluid dynamics and blood platelet, ASME J. Biomech. Eng. 118 (1996) 280–286.
[21] R. Budwig, D. Elger, H. Hooper, J. Slippy, Steady flow in abdominal aortic aneurysm models, ASME J. Biomech. Eng. 115 (1993) 419–423.
[22] C.L. Asbury, J.W. Rwberti, E.I. Bluth, R.A. Peattie, Experimental investigation of steady flow in rigid models of abdominal aortic aneurysm, Ann. Biomed. Eng. 23 (1995) 29–39.
[23] R.A. Peattie, T.J. Riehle, E.I. Bluth, Pulsatile flow in fusiform models of abdominal aortic aneurysms: Flow fields, velocity patterns and flow-induced wall stresses, ASME J. Biomech. Eng. 126 (2004) 438–446.
[24] T.H. Yip, S.C.M. Yu, Cyclic transition to turbulence in rigid abdominal aortic aneurysm models, Fluid Dynam. Res. 29 (2001) 81–113.
[25] T.H. Yip, S.C.M. Yu, Oscillatory flows in straight tubes with an axisymmetric bulge, Exp. Thermal Fluid Sci. 26 (2002) 947–961.
[26] J.A. Ekaterinaris, C.V. Ioannou, A.N. Katsamouris, Flow dynamics in expansions characterizing abdominal aorta aneurysms, Ann Vasc. Surg. 20 (2006) 351–359.
[27] R. Berguer, J.L. Bull, K.M. Khanafer, Refinements in Mathematical models to predict aneurysm growth and rupture, Ann. New York Acad. Sci. 1085 (2006) 110–116.

[28] K.M. Khanafer, J.L. Bull, G.R. Upchurch, R. Berguer, Turbulence significantly increases pressure and fluid shear stress in an aortic aneurysm model under resting and exercise flow conditions, Ann. Vasc. Surg. 21 (2007) 67–74.
[29] P.F. Davies, A. Remuzzi, E.J. Gordon, C.F. Dewey Jr., M.A. Gimbrone Jr., Turbulent fluid shear stress induces vascular endothelial cell turnover in vitro, Proc. Natl. Acad. Sci. USA 83 (1986) 2114–2117.
[30] D.N. Ku, D.P. Giddens, C.K. Zarins, S. Glagov, Pulsatile flow and atherosclerosis in the human carotid bifurcation: Positive correlation between plaque location and low oscillating stress, Arteriosclerosis 5 (1985) 293–302.
[31] Y.C. Fung, Biomechanics: Mechanical Properties of Living Tissues, Springer-Verlag, New York, 1993.
[32] T. Fukushima, T. Matsuzawa, T. Homma, Visualization and finite element analysis of pulsatile flow in models of the abdominal aortic aneurysm, Biorheology 26 (1998) 109–130.
[33] M.L. Raghavan, J. Kratzberg, E.M. Castro de Tolosa, M.N. Hanaoka, P. Walker, E.S. da Silva, Regional distribution of wall thickness and failure properties of human abdominal aortic aneurysm, J. Biomech. 39 (2006) 3010–3016.
[34] D.A. Vorp, M.L. Raghavan, M.W. Webster, Mechanical wall stress in abdominal aortic aneurysm: influence of diameter and asymmetry, J. Vasc. Surg. 27 (1998) 632–639.
[35] M.J. Thubrikar, M. Labrosse, F. Robicesk, J. Al-Soudi, B. Fowler, Mechanical properties of abdominal aortic aneurysm wall, J. Med. Eng. Technol. 25 (2001) 133–142.
[36] M.L. Raghavan, D.A. Vorp, Toward a biomechanical tool to evaluate rupture potential of abdominal aortic aneurysm: identification of a finite strain constitutive model and evaluation of its applicability, J. Biomech. 33 (2000) 475–482, 2000.
[37] C. Mills, I. Gabe, J. Gault, D. Mason, J. Ross, E. Braumwald, J. Shillingford, Pressure-flow relationships and vascular impedance in man, Cardiovasc. Res. 4 (1970) 405–417.
[38] D.C. Wilcox, Simulation of transition with a two-equation turbulence model, AIAA J. 32 (1994) 247–255.
[39] J. Ryval, A.G. Straatman, D.A. Steinman, Two-equation turbulence modeling of pulsatile flow in a stenosed tube, J. Biomech. Eng. 126 (2004) 625–635.
[40] S.S. Varghese, S.H. Frankel, Numerical modeling of pulsatile turbulent flow in stenotic vessels, J. Biomech. Eng. 125 (2003) 445–460.
[41] F. Ghalichi, X. Deng, A. De Champlain, Y. Douville, M. King, R. Guidoin, Low Reynolds number turbulence modeling of blood flow in arterial stenoses, Biorheology 35 (1998) 281–294.
[42] T.S. Lee, W. Liao, H.T. Low, Numerical simulation of turbulent flow through series stenoses, Int. J. Numer. Methods Fluids 42 (2003) 717–740.
[43] C.M. Harris, Shock and Vibration Handbook, third ed., McGraw-Hill Book Company, 1988, (Chapter 29, Section "Internal Flow in Pipes").
[44] V.G. Priymak, T. Miyazakiy, Accurate Navier–Stokes investigation of transitional and turbulent flows in a circular pipe, J. Comput. Phys. 142 (1998) 370–411.
[45] L. Shemer, I. Wygnanski, E. Kit, Pulsating flow in a pipe, J. Fluid Mech. 153 (1985) 313–337.
[46] V. Deplano, Y. Knapp, E. Bertrand, E. Gaillard, Flow behavior in an asymmetric compliant experimental model for abdominal aortic aneurysm, J. Biomech. 40 (2007) 2406–2413.
[47] J.S. Liu, P.C. Lu, Turbulence characteristics downstream of bileaflet aortic valve prostheses, ASME, J. Biomech. Eng. 122 (2000) 118–124.